



Cite this: *CrystEngComm*, 2024, 26, 4592

## Investigation of visible emission and luminescence center evolution in Pr–La:CaF<sub>2</sub> single crystals for laser application

Chonglei Xu,<sup>ab</sup> Fengkai Ma,<sup>\*c</sup> Zhen Zhang,<sup>ab</sup> Zhonghan Zhang,<sup>ab</sup> Huamin Kou<sup>ab</sup> and Liangbi Su <sup>\*ab</sup>

A series of Pr,La:CaF<sub>2</sub> single crystals grown using the temperature gradient technique (TGT) method were presented systematically with a detailed spectroscopic investigation. The results indicate that the distinct Pr<sup>3+</sup>–La<sup>3+</sup> cluster types have replaced the original Pr<sup>3+</sup>–Pr<sup>3+</sup> clusters after introducing La<sup>3+</sup> into the Pr:CaF<sub>2</sub> crystal, as demonstrated by density functional theory-based first principles calculation and spectral analysis. This cluster evolution has led to a drastic increase in the Pr<sup>3+</sup> emission quantum efficiency as the La<sup>3+</sup> concentration increases. Evaluation of the impacts of multiphonon relaxation and cross-relaxation processes on quantum yields also revealed that cross-relaxation processes persisted in the Pr, La co-doped samples, which led to not high quantum yields as expected. The incorporation of La<sup>3+</sup> substantially manipulated the local structure of Pr ions in the CaF<sub>2</sub> crystal lattice. Low temperature absorption and selective-site spectroscopy, and time resolved emission spectroscopy were applied to investigate the local structure symmetries of Pr ions in the Pr<sup>3+</sup>,La<sup>3+</sup>:CaF<sub>2</sub> crystal. Despite a lower degree of discrepancy, two types of centers were observed in TRES, all of which showed cubic symmetry of these locations based on the cluster simulation.

Received 11th March 2024,  
Accepted 6th July 2024

DOI: 10.1039/d4ce00246f

[rsc.li/crystengcomm](https://rsc.li/crystengcomm)

### 1. Introduction

Trivalent praseodymium is a particularly fascinating lanthanide ion due to its many visible and infrared transitions. In recent years, there has been an increasing interest in Pr<sup>3+</sup> doped laser systems due to the development of blue GaN laser diode pump sources, which perfectly match specific Pr<sup>3+</sup> absorption lines. The green, orange, and red transitions of Pr<sup>3+</sup> have already been utilized in laser materials like Pr<sup>3+</sup>:LiYF<sub>4</sub> and Pr<sup>3+</sup>:SrAl<sub>12</sub>O<sub>19</sub>.<sup>1–4</sup>

Among the fluorides, CaF<sub>2</sub> with an optically isotropic fluorite structure has a broad transparency spectrum range that extends into the UV region, high thermal conductivity, and a low maximum phonon energy of around 320 cm<sup>–1</sup>, which significantly limits non-radiative transitions. These properties make this material useful for a wide range of optical applications. However, the Pr<sup>3+</sup>:CaF<sub>2</sub> crystal as a laser system has been shelved for a long time due to a very

negative concentration quenching effect caused by Pr<sup>3+</sup> ion clustering and certain cross-relaxation energy transfer processes that reduce their emission quantum efficiency. To overcome this disadvantage, it has been suggested to co-dope with non-optically active ions in order to create new clusters around single Pr<sup>3+</sup> ions, isolating them from one another. Pr:CaF<sub>2</sub> co-doped with Gd<sup>3+</sup> ions has been studied and continuous-wave laser generation has already been demonstrated, with a maximum output power of 22 mW at 642 nm.<sup>5</sup> Then in a Pr<sup>3+</sup>,Gd<sup>3+</sup>:SrF<sub>2</sub> crystal, a slope efficiency of 4.4% was reached with a maximum output power of 47 mW at 605.98 nm.<sup>6</sup> Another promising candidate is Lu<sup>3+</sup> which also efficiently breaks Pr<sup>3+</sup> clusters and paves the way towards the development of a Pr<sup>3+</sup> doped CaF<sub>2</sub> visible laser.<sup>7</sup> While the spectrum properties and laser performance have improved significantly, there is still uncertainty regarding the sites of Pr<sup>3+</sup> or Lu<sup>3+</sup> non-optically active ions. Comparably, we incorporated La for the first time in this research to regulate local structure, mostly because of the similar ionic radii of Pr<sup>3+</sup> and La<sup>3+</sup>, and the computed findings indicate that Pr<sup>3+</sup> and La<sup>3+</sup> may form clusters with a similar degree of ease.

The insertion of trivalent rare-earth ions into the fluorite structure is well known to be accompanied by charge-compensating defects that result in various types of centers consisting of one rare-earth ion or many rare-earth ions within a cluster. Numerous studies have been conducted to

<sup>a</sup> State Key Laboratory of High Performance Ceramics and Superfine Microstructure, Shanghai Institute of Ceramics, Chinese Academy of Sciences, Shanghai 201899, China. E-mail: [suliangbi@mail.sic.ac.cn](mailto:suliangbi@mail.sic.ac.cn)

<sup>b</sup> Center of Materials Science and Optoelectronics Engineering, University of Chinese Academy of Sciences, Beijing 100049, China

<sup>c</sup> Department of Optoelectronic Engineering, Jinan University, Guangzhou 510632, China. E-mail: [mafengkai@jnu.edu.cn](mailto:mafengkai@jnu.edu.cn)

investigate the theoretical and experimental aspects of these integration sites. Clustering in rare-earth-doped calcium fluoride has been shown to be substantial even at low dopant concentrations, such as 0.05% Pr<sup>3+</sup>.<sup>8</sup> The possibility of energetically favorable aggregates or rare-earth (RE) clusters forming in CaF<sub>2</sub> was initially proposed in 1964.<sup>9</sup> Since then, following a wide number of structural studies based on experimental techniques such as electron paramagnetic resonance spectroscopy (EPR),<sup>10,11</sup> nuclear magnetic resonance (NMR),<sup>12</sup> dielectric relaxation spectroscopy (DRS),<sup>13</sup> and extended X-ray absorption fine structure (EXAFS)<sup>14</sup> as well as computer simulations.<sup>15</sup> It was concluded that charge compensation could be achieved in several ways depending on the rare-earth size, the lattice parameter, the doping concentration and the sample thermal treatments. However, despite the use of a variety of experimental methodologies, a clear description of these defects has not yet been generated. Tissue and Wright<sup>16</sup> described up to 22 different sites for 0.1% Pr<sup>3+</sup> in CaF<sub>2</sub>, of which only three were assigned to single ions, leaving the remaining 19 sites identified as cluster sites composed of two (pairs or dimers) or three (trimer) ions. Consequently, Pr<sup>3+</sup> clustering causes the visible emission from <sup>3</sup>P<sub>0</sub> in CaF<sub>2</sub> to be extremely weak. In order to expand the usage of rare-earth doped CaF<sub>2</sub> to photonic applications, it is thus highly appealing to find strategies to prevent the development of rare-earth clusters in Pr<sup>3+</sup>:CaF<sub>2</sub>. To the best of our knowledge, however, there is no conclusive evidence that these co-dopants significantly hinder the development of rare-earth clusters and generate new luminescence centers.

This study shows that the co-doping of Pr<sup>3+</sup> with La<sup>3+</sup> ions can effectively prevent the formation of Pr<sup>3+</sup> clusters by forming clusters made up of Pr<sup>3+</sup> and La<sup>3+</sup> centers. Compared to singly doped Pr<sup>3+</sup>:CaF<sub>2</sub>, a significantly increase in praseodymium visible luminescence is observed in Pr<sup>3+</sup>, La<sup>3+</sup> co-doped CaF<sub>2</sub>, which could potentially lead to visible laser operation. On the other hand, we continued to perform low temperature selective site spectroscopy and time-resolved emission spectroscopy (TRES) to learn more about the new luminescence center. Additionally, a density functional theory (DFT) based first principles calculations were carried out for the Pr<sup>3+</sup>, La<sup>3+</sup> doped CaF<sub>2</sub>, giving us a clear picture of the cluster characters.

## 2. Experimental setup

### 2.1 Experiments for crystal growth and spectra properties

0.6 at% Pr<sup>3+</sup>:CaF<sub>2</sub> (0.6Pr) as well as 0.6 at% Pr<sup>3+</sup>, *x* at% La<sup>3+</sup>:CaF<sub>2</sub> crystals (*x* = 1, 6, 9, 15, 20; 0.6Pr,1La; 0.6Pr,6La; 0.6Pr,9La; 0.6Pr,15La; 0.6Pr,20La) were fabricated using the TGT method. In addition, a series of 0.05% Pr-doped samples were also grown for the purpose of measuring the radiative lifetimes. The raw materials PrF<sub>3</sub> (99.99%), LaF<sub>3</sub> (99.99%), CaF<sub>2</sub> (99.99%) and PbF<sub>2</sub> (99.99%) were initially added to a growing chamber in a graphite crucible, which was then heated slightly above (~30–50 °C) the melting point and the

solution was homogenized for 24 hours. The pressure within the furnace chamber was maintained below  $5 \times 10^{-3}$  Pa during the crystal growth process. For spectroscopic characterization, the as-grown crystals were sliced to a thickness of 2 mm and double-sided polished.

An Agilent UV-VIS-IR spectrophotometer (Cary-5000) was used to detect the absorption of samples. Additionally, an FLS-1000 photoluminescence spectrometer with Red-PMT is used to gather the luminescence spectra under a Xe lamp excited at 443 nm. We used the same excitation and emission slit widths to record the emission spectra. This ensured consistent measurement conditions across different concentration samples, providing reliable results for spectral comparisons. Since each sample was prepared with a thickness of 2 mm, extra care was needed to ensure that they were all identical in shape. The tiny thickness of the samples is crucial to achieving an equal excitation beam profile within each sample since the samples may show differing absorption cross-sections at the excitation wavelength. It is possible to compare the emission intensities of the several samples directly by maintaining the same experimental setup for each sample. We used an optical parametric oscillator powered by the third harmonic (355 nm) of a Nd<sup>3+</sup>:YAG laser to perform emission decays and time-resolved spectra. Low temperature (*T* = 77 K) measurements were carried out using an East Changing liquid nitrogen cryostat coupled with an East Changing TC 202 temperature controller. Using an inductively coupled plasma optical emission spectrometer (ICP-OES), the actual concentration of Pr<sup>3+</sup> was determined.

### 2.2 Computational procedure in VASP

The first-principles calculations based on DFT are performed by the plane-wave basis set method using the VASP code. The interactions between electrons and ions were described by the projector augmented wave (PAW) potential. Furthermore, all computations took the spin polarization into account. The relaxation was verified to have an accuracy of  $10^{-5}$  eV using a  $1 \times 1 \times 1$  gamma *k*-grid and a 550 eV cut-off in the plane-wave expansion. To achieve enough precision, the internal coordinates of the  $2 \times 2 \times 2$  supercell were refined until the forces exerted on individual atoms approached  $0.01 \text{ eV } \text{Å}^{-1}$ . The formation energy ( $\Delta E$ ) of the cluster was calculated using the following formula:<sup>17</sup>

$$\Delta E = (E_{\text{tot}} + E_0) - i \cdot E_1 - (s - \nu) \cdot E_2 - \{[i + (s - \nu)] - [i - (s - \nu)^2]\} \cdot E_{\text{corr}}$$

where  $E_{\text{tot}}$  denotes the total relaxed energy of the centers with notation of  $i|v|d|s_r\text{-O}$ ; *i* is the number of trivalent substitutional impurities, *ν* is the number of lattice anion vacancies, *d* is the number of anions that deviated from the normal lattice site, *s* is the number of interstitials at the nearest (*r* = 1) or next nearest site (*r* = 2), and “O” is the shape of the cluster configuration;  $E_0$  is the energy of pure CaF<sub>2</sub> crystal;  $E_1$  and  $E_2$  respectively are the relaxed energy of

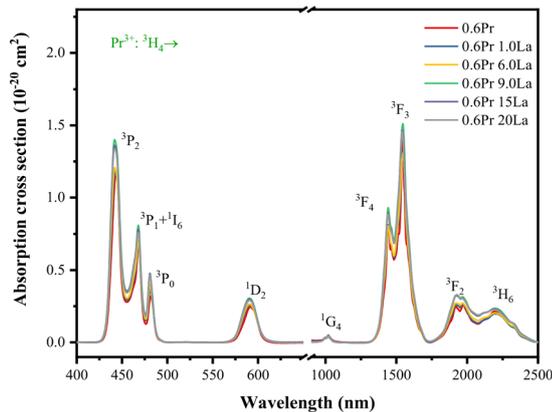


Fig. 1 Absorption spectra of the Pr,L:CaF<sub>2</sub> crystal.

the centers  $1|0|0|0$  and  $0|0|0|1$  in a  $2 \times 2 \times 2$  supercell;  $E_{\text{corr}}$  is the potential alignment and charge corrections calculated by following equation:

$$E_{\text{corr}} = (1 + g) \frac{q^2 \alpha}{2\epsilon L}$$

where  $q$  is the net charge,  $\alpha$  is the Madelung constant of 5.0388,  $\epsilon$  is the static electric constant,  $L$  represents the supercell dimensions ( $2 \times 2 \times 2$ ) of CaF<sub>2</sub> and  $g$  is the scaling factor (a value of  $-0.34$  was chosen for the face-centered cubic structure). The computed  $E_{\text{corr}}$  for a  $2 \times 2 \times 2$  supercell of CaF<sub>2</sub> crystal with a net charge of  $q = 1$  was 0.323 eV.

## 3. Results and discussion

### 3.1 Spectroscopic properties

Fig. 1 shows the results of the identification and assignment of the absorption bands in the vis-IR range. The room-temperature absorption spectra of Pr,L:CaF<sub>2</sub> and the singly doped with Pr<sup>3+</sup> sample were obtained. These spectra are mostly made up of several bands in the entire visible and near-infrared regions that correspond to  $^3\text{H}_4 \rightarrow ^3\text{P}_2$ ,  $^3\text{P}_1 + ^1\text{I}_6$ ,  $^3\text{P}_0$ ,  $^1\text{D}_2$ ,  $^1\text{G}_4$ ,  $^3\text{F}_{3,4}$ , and  $^3\text{F}_2 + ^3\text{H}_6$  respectively. The majority of these transitions are electric dipole ones; the only ones with magnetic dipole contribution are  $^3\text{H}_4 \rightarrow ^1\text{G}_4$  and  $^3\text{F}_{4,3}$ . It is noteworthy to notice that the most powerful transition  $^3\text{H}_4 \rightarrow ^3\text{P}_2$  corresponds to the 444 nm absorption associated with Pr<sup>3+</sup> ions. Its bandwidth is approximately ten nanometers greater than that of YLF, making it ideal for pumping with a specific wavelength range.

The excitation and emission channels in the Pr-doped crystal are shown in Fig. 2. After excitation to the  $^3\text{P}_2$  level at *ca.* 443 nm, the electrons undergo non-radiative relaxation to populate the lower-lying steady-state levels ( $^3\text{P}_0$ ,  $^3\text{P}_1$ ,  $^1\text{I}_6$ ). This relaxation process subsequently leads to the observed emission spectrum, which consists of six bands in the visible region. The emission bands located at 483, 524, 606, 639, 702, and 721 nm correspond to the transitions from the  $^3\text{P}_0$  or  $^3\text{P}_1$  level to the  $^3\text{H}_4$ ,  $^3\text{H}_5$ ,  $^3\text{H}_6$ ,  $^3\text{F}_2$ , and  $^3\text{F}_{3,4}$  levels,

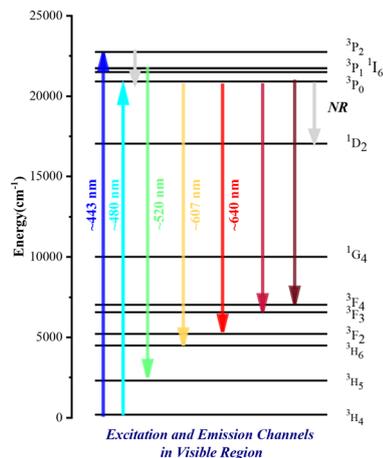
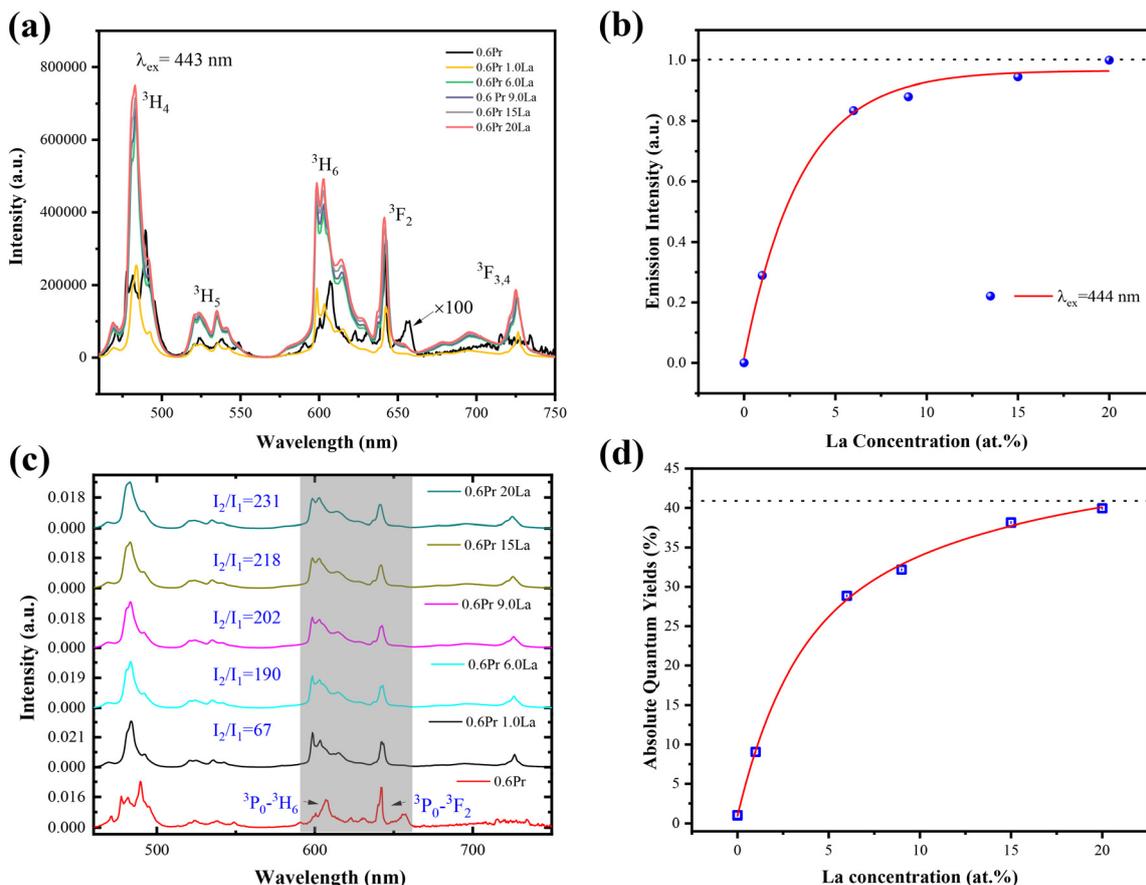


Fig. 2 The excitation and emission channels in the Pr-doped CaF<sub>2</sub> crystal.

respectively. The comprehensive analysis of this emission spectrum provides valuable insights into the energy level structure and radiative transitions of the Pr<sup>3+</sup> ions within the CaF<sub>2</sub> host crystal.

The identification and assignment of the emission bands in the visible region have been performed and it can be seen in Fig. 3(a) under excitation at 443 nm. The emission intensity of the  $^3\text{P}_0 \rightarrow ^3\text{H}_6$  transition increases with the La concentration up to more than several hundred times the initial value for the Pr<sup>3+</sup> singly doped sample, which is clear evidence of the breaking of Pr<sup>3+</sup>-Pr<sup>3+</sup> clusters by co-doping. In contrast, the extremely weak Pr<sup>3+</sup> emission seen in Pr<sup>3+</sup>:CaF<sub>2</sub> compared to Pr,L:CaF<sub>2</sub> shows that the majority of Pr<sup>3+</sup> ions are aggregated together and that the Pr<sup>3+</sup> emission is suppressed within these clusters. The initial Pr<sup>3+</sup>-Pr<sup>3+</sup> clusters are therefore replaced in the matrix host by Pr<sup>3+</sup>-La<sup>3+</sup> clusters which prevent the onset of the cross relaxation process quenching the Pr<sup>3+</sup> luminescence.<sup>7</sup> Plotting the integrated emission intensity of  $^3\text{P}_0 \rightarrow ^3\text{H}_6, ^3\text{F}_2$  against La<sup>3+</sup> concentration in Fig. 3(b) reveals that the rise follows a cumulative distribution function curve, reaching an asymptotic value. Thus, the incorporation of La<sup>3+</sup> as a co-dopant somehow modifies the clustering structure of Pr<sup>3+</sup> ions with the consequence of preventing the formation of Pr<sup>3+</sup> clusters. The visible region quantum efficiency of the  $^3\text{P}_0$  level increases drastically with the La<sup>3+</sup> concentration simultaneously as shown in Fig. 3(d). For all samples, emission intensities were integrated across the wavelength range of 570 to 660 nm. Fig. 3(c) shows the ratio  $I_2/I_1$  between the integrated intensities, with sample "1" being 0.6% Pr<sup>3+</sup>:CaF<sub>2</sub> and sample "2" being the Pr,L:CaF<sub>2</sub> samples. Between the two samples, an intensity ratio of 231 ( $I_2/I_1$ ) is seen, indicating that 0.6Pr<sup>3+</sup>,20La<sup>3+</sup>:CaF<sub>2</sub> is 231 times brighter compared to 0.6Pr<sup>3+</sup>:CaF<sub>2</sub>. Since the absorption coefficients ( $\alpha = \sigma_{\text{abs}}N$ ) at the pumping wavelength are 1.6 cm<sup>-1</sup> and 1.5 cm<sup>-1</sup> in 0.6% Pr<sup>3+</sup>:CaF<sub>2</sub> and 0.6Pr<sup>3+</sup>,20La<sup>3+</sup>:CaF<sub>2</sub>, respectively, this finding cannot be explained by differences in absorption.



**Fig. 3** (a) Emission spectra of Pr<sup>3+</sup> <sup>3</sup>P<sub>0</sub> level when excited at 443 nm. (c) Normalized spectra have an integrated intensity equal to one for sake of clarity. The gray boxes represent the integral areas. (b) and (d) <sup>3</sup>P<sub>0</sub>-<sup>3</sup>H<sub>6</sub>, <sup>3</sup>F<sub>2</sub> integrated emission intensity and quantum efficiency of the Pr,L:CaF<sub>2</sub> sample versus La<sup>3+</sup> co-dopant concentration.

The primary distinction between the rare-earth incorporation sites in different hosts leads to this outcome. Unlike single-site fluoride hosts with a uniform distribution of dopants within the lattice such as LiYF<sub>4</sub>,<sup>18</sup> strong emission quenching due to the clustering effect of Pr<sup>3+</sup>:CaF<sub>2</sub> is to be expected. In conclusion, the Pr<sup>3+</sup> emission recorded in 0.6Pr:CaF<sub>2</sub> exclusively arises from a minority of “isolated” Pr<sup>3+</sup> ions, which can be identified as corresponding to the C<sub>4v</sub> single ion sites when compared with the literature.<sup>16</sup> The short distance between the Pr<sup>3+</sup> ions in clusters clearly favor cross-relaxation processes. For Pr<sup>3+</sup> ions, there are many cross-relaxation pathways that include the energy transfer between an excited Pr<sup>3+</sup> ion in the <sup>3</sup>P<sub>0</sub> multiplets and a Pr<sup>3+</sup> ion in the <sup>3</sup>H<sub>4</sub> ground state resulting in decay non-radiatively through multiphonon emission or emission of an infrared photon.<sup>19</sup> Therefore, the co-doping of Pr<sup>3+</sup> with La<sup>3+</sup> has been shown to be an effective way to avoid the formation of Pr<sup>3+</sup>-Pr<sup>3+</sup> clusters.

The ratio of intensities I<sub>2</sub>/I<sub>1</sub> is directly correlated with the ratio of emitting center concentrations N<sub>2</sub>/N<sub>1</sub>. N<sub>i</sub> is the concentration of emitting centers in sample *i*. Since the fraction of emitting centers in Pr-Pr clusters is so low, we will disregard it in this instance and go into further explanation

in the following section. Effective emitting centers are denoted by N<sub>i</sub> and are restricted to isolated Pr ions that do not quench for consideration. As long as the concentration of excited ions is low to prevent any depletion of the ground state, it is possible to precisely define the connection between emission strength and the number of emitting centers.<sup>7</sup> The rate equation for the concentration of luminescence centers in the excited state n(<sup>3</sup>P<sub>0</sub>) changes into:

$$\frac{dn(^3P_0)}{dt} = -\frac{n(^3P_0)}{\tau(^3P_0)} + \sigma_{\text{abs}}\phi N_{\text{Pr}} \quad (3-1)$$

In the steady-state regime (dn(<sup>3</sup>P<sub>0</sub>)/dt = 0), the concentration of emitting centers in the excited state n(<sup>3</sup>P<sub>0</sub>) is then simply given by

$$n(^3P_0) = \sigma_{\text{abs}}\phi N_{\text{Pr}}\tau(^3P_0) \quad (3-2)$$

where N<sub>Pr</sub> represents the total concentration of emitting centers, σ<sub>abs</sub> is the absorption cross-section; φ is the excitation photon flux and τ(<sup>3</sup>P<sub>0</sub>) is the emitting level lifetime. On the other hand, the emission intensity is proportional to the concentration of emitting centers in the excited state n(<sup>3</sup>P<sub>0</sub>) as follows:

$$I \propto \frac{\beta \times n(^3P_0)}{\tau_{\text{rad}}(^3P_0)} \quad (3-3)$$

where  $\tau_{\text{rad}}$  is the level emission radiative lifetime and  $\beta$  is the branching ratio of the transition (or transitions) under consideration. Given that the photon flux  $\Phi$  is constant for all samples, one may calculate the ratio of emitting center concentrations as a function of the intensity ratio  $I_2/I_1$  by combining eqn (3-2) and (3-3):

$$\frac{N_2}{N_1} = \frac{I_2 \beta_1 \sigma_{\text{abs}1} \tau_1 \tau_{\text{rad}2}}{I_1 \beta_2 \sigma_{\text{abs}2} \tau_2 \tau_{\text{rad}1}} \quad (3-4)$$

Table 1 provides a summary of the experimentally measured values required to perform the computations in eqn (3-4). By capturing the complete  $^3P_0$  emission spectrum from 480 nm to 800 nm and correcting for the experimental spectral response, the branching ratio  $\beta$  of the red ( $^3P_0 \rightarrow ^3F_2$ ) and orange ( $^3P_0 \rightarrow ^3H_6$ ) transitions was determined. Since the  $^3P_0 \rightarrow ^1D_2, ^1G_4$  infrared transition contributes very little to the total emission spectrum, it was not considered.<sup>20</sup> Subsequently, the branching ratio  $\beta$  was computed by dividing the spectral integral of the emission spectrum by the spectral integral of the red and orange transitions of interest.

The luminescence kinetics of  $\text{Pr}^{3+}$  ions in the investigated materials is strongly related to the presence of  $\text{La}^{3+}$ . Fig. 3(a) compares semilog plots of  $^3P_0$  luminescence decay curves recorded at room temperature for the  $\text{CaF}_2$  crystal containing 0.6 at%  $\text{Pr}^{3+}$  sample series. The lifetimes were determined by normalizing to unity the decay curves at  $t = 0$  and by integrating the entire decay curves.<sup>21</sup> In the 0.6Pr:CaF<sub>2</sub> sample, the decays approximately follow a double-exponential trend over two orders of magnitude and has a fast decay component apparently as a consequence of strong cross relaxation interaction between the  $\text{Pr}^{3+}$ - $\text{Pr}^{3+}$  cluster with a time constant substantially exceeding the time range covered in our experiments. What is going on in this sample is that, due to the formation of clusters in this host, we find two main species of Pr ions, one is in the form of a Pr cluster which do not emit light at all due to strong quenching corresponding to the short part (0.58  $\mu\text{s}$ ), and the other one which are isolated Pr ions giving the long lifetime part (142  $\mu\text{s}$ ). The calculated proportion of the short lifetime  $\phi$ , quantum yield of luminescence in the cluster  $\eta_{\text{cluster}}$  and the proportion of cluster  $R_{\text{cluster}}$  can be expressed as the following formulas:

$$\begin{aligned} \phi &= \frac{A_s \tau_s}{A_s \tau_s + A_l \tau_l} \\ \eta_{\text{cluster}} &= \frac{\sigma_r}{\sigma_r + \sigma_{\text{nr}}} = \frac{\tau_s}{\tau_{\text{rad}}} \\ R_{\text{cluster}} &= \frac{\phi / \eta_{\text{cluster}}}{\phi / \eta_{\text{cluster}} + (1 - \phi)} = \frac{\phi \tau_{\text{rad}}}{\phi \tau_{\text{rad}} + (1 - \phi) \tau_s} \end{aligned} \quad (3-5)$$

where  $A_s$  and  $A_l$  are the fitting constants of the equations;  $\tau_s$  and  $\tau_l$  are the short lifetime and long lifetime part, respectively;  $\sigma_r$  and  $\sigma_{\text{nr}}$  are the transition rates of radiative and non-radiative processes. The calculated proportion of short lifetime  $\phi$  is 0.01 in 0.6Pr:CaF<sub>2</sub>, and quantum yield of luminescence in the cluster  $\eta_{\text{cluster}}$  is about 0.01 ( $\tau_s = 0.58 \mu\text{s}$  shown in Fig. 4(a),  $\tau_{\text{rad}} = 54 \mu\text{s}$  in Fig. 4(c)). As a result, the proportion of the cluster  $R_{\text{cluster}}$  is 50% in 0.6Pr:CaF<sub>2</sub>.

By adding lanthanum, the non-emitting  $\text{Pr}^{3+}$ - $\text{Pr}^{3+}$  clusters were replaced by Pr-La luminescence centers, which begin to dominate the decay and emit, providing an approximate lifetime of 36  $\mu\text{s}$  as shown in Fig. 4(b). We believe that there is still some quenching in these clusters due to the low quantum efficiency as shown in Fig. 3(d) and the longer lifetime of 0.05Pr,5La:CaF<sub>2</sub>.

The radiative lifetimes are usually derived using the Judd-Ofelt theory. However, this calculation does not give satisfying results in the case of  $\text{Pr}^{3+}$  doped multisite systems since one should isolate for each  $\text{Pr}^{3+}$ - $\text{La}^{3+}$  cluster a separate set of absorption spectra.<sup>21</sup> Therefore, we derived the  $^3P_0$  radiative lifetimes by adding enough of the  $\text{La}^{3+}$  ions so as to avoid any possible cross-relaxation processes. The content of La ions is several hundred times that of Pr, it can be assumed that at this time Pr is completely evenly distributed within the lattice. In addition, since the ion radius of La is comparable to the Pr ion, there should be a comparable agglomeration tendency, and the cluster structure properties should develop similarly. This hypothesis will be detailed by DFT calculation in the next section. Consequently, this estimation of the radiative lifetime is valid provided that energy transfer does not exist in Fig. 3(b). The radiative lifetime for the 0.6Pr sample series presented in Table 1 should correspond to the lifetime of the 0.05Pr,10La sample displayed in Fig. 3(b). The radiative lifetime in 0.6Pr:CaF<sub>2</sub> is expected to be equal to the lifetime in 0.05Pr:CaF<sub>2</sub>.

The significant number of non-emitting  $\text{Pr}^{3+}$  clusters in 0.6Pr:CaF<sub>2</sub> is confirmed by the results in Table 1, which show that the number of  $\text{Pr}^{3+}$  emitting centers is 180 times bigger

**Table 1** Spectroscopic parameters applied in eqn (3-4) computations in the Pr,La:CaF<sub>2</sub> sample. The red ( $^3P_0 \rightarrow ^3F_2$ ) and orange ( $^3P_0 \rightarrow ^3H_6$ ) transitions branching ratio is denoted by  $\beta$ ; the effective absorption cross-section is represented by  $\sigma_{\text{abs}}$ ;  $\tau$  and  $\tau_{\text{rad}}$  are the measured and radiative lifetime of the  $^3P_0$  level respectively

Sample	$\beta$	$\sigma_{\text{abs}}$ ( $10^{-21} \text{ cm}^2$ )	$\tau(^3P_0)$ ( $\mu\text{s}$ )	$\tau_{\text{rad}}(^3P_0)$ ( $\mu\text{s}$ )	$I_2/I_1$	$N_2/N_1$
0.6Pr:CaF <sub>2</sub>	0.38	1.15	122	172	—	—
0.6Pr 1.0La	0.469	1.16	34	54	67	58
0.6Pr 6.0La	0.466	1.17	36	55	190	157
0.6Pr 9.0La	0.462	1.18	36	55	202	167
0.6Pr 15La	0.462	1.20	38	55	218	169
0.6Pr 20La	0.462	1.20	38	55	231	180

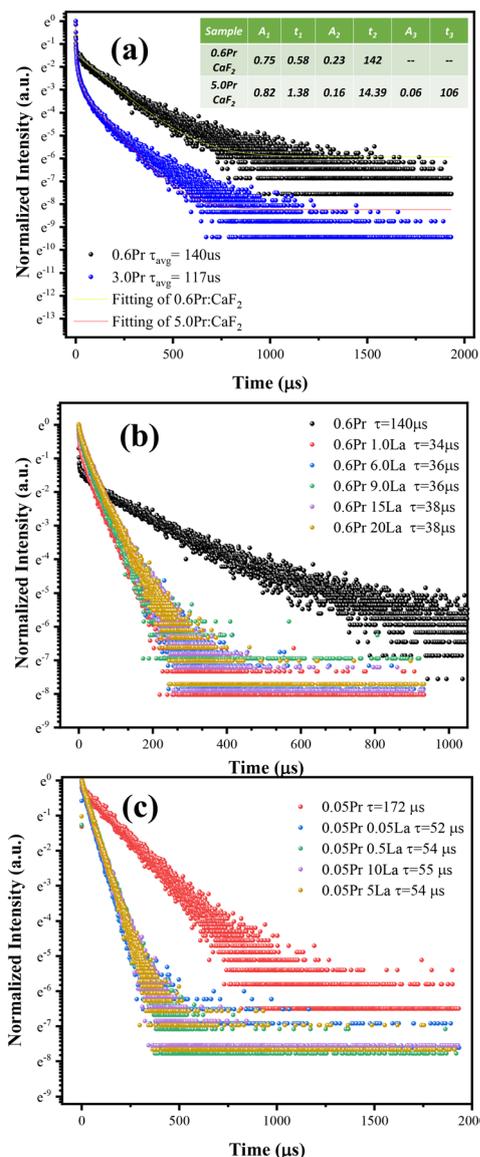


Fig. 4  $^3P_0$  fluorescence decay curves of the Pr,L:CaF<sub>2</sub> crystal under pulsed excitation at 443 nm. (a) 0.6Pr and 5.0Pr doped CaF<sub>2</sub> samples, (b) 0.6% Pr sample series, (c) 0.05% Pr sample series.

in 0.6Pr,20La:CaF<sub>2</sub> than in 0.6Pr:CaF<sub>2</sub> for an approximately equivalent concentration of Pr<sup>3+</sup> ions. The quantum efficiency of  $^3P_0$  and the calculated  $N_2/N_1$  are shown as a function of La<sup>3+</sup> concentration in Fig. 5(a). When co-doping Pr<sup>3+</sup> with La<sup>3+</sup> in CaF<sub>2</sub>, the number of luminescence centers increases drastically, along with the quantum efficiency, demonstrating that the co-dopant allows previously non-emitting Pr<sup>3+</sup> centers to generate visible emission by taking the place of Pr<sup>3+</sup> ions inside the Pr<sup>3+</sup> clusters. Nonetheless, the quantum efficiency of Pr,L:CaF<sub>2</sub> is not as high as expected, there maybe some process caused the energy dissipation of  $^3P_0$  level. The following modified exponential energy-gap law of Van Dijk and Schuurmans could be used to compute the multiphonon relaxation rate,<sup>22</sup> given that the energy gap between  $^3P_0$  and  $^1D_2$  is roughly 3500 cm<sup>-1</sup>:

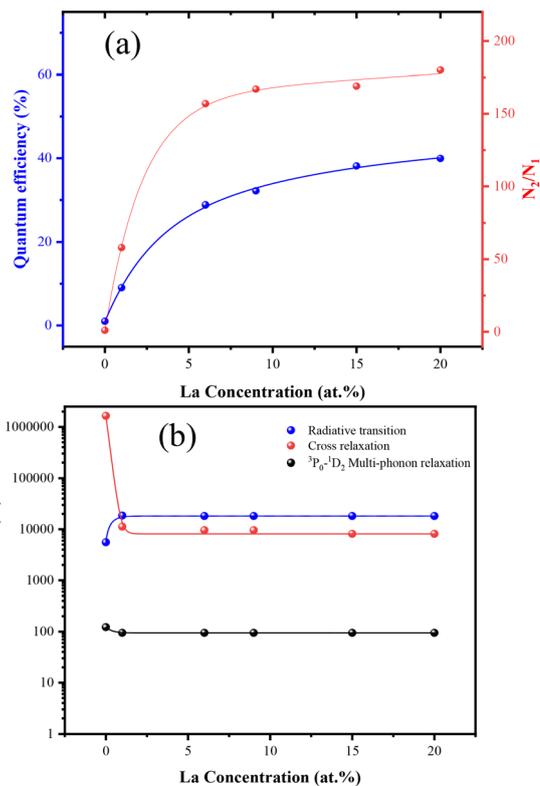


Fig. 5 (a) Emission quantum efficiency of  $^3P_0$  at room temperature and calculated  $N_2/N_1$  versus La<sup>3+</sup> concentration; (b) evolution of the radiative transition rate, cross relaxation rate and  $^3P_0$ - $^1D_2$  multi-phonon relaxation rate as a function of La<sup>3+</sup> concentration in 0.6% Pr<sup>3+</sup>,xLa<sup>3+</sup>:CaF<sub>2</sub> (x = 1, 6, 9, 15, 20).

$$W_{\text{MPR}}(T = 0 \text{ K}) = \beta_{\text{el}} \exp[-\alpha(\Delta E - 2\hbar\omega_{\text{max}})] \quad (3-6)$$

The total radiative rate of the  $^3P_0$  state is calculated with the radiative lifetime as shown in Fig. 5(b), which is typically  $2 \times 10^4 \text{ s}^{-1}$  for fluoride such as LiYF<sub>4</sub>.<sup>23</sup> We conclude that the multiphonon relaxation rate is  $10^2 \text{ s}^{-1}$ , which is 200 times smaller than the radiative rate. Consequently, the multiphonon relaxation mechanism is insufficient to explain the approximately 40% quantum efficiency. On the other hand, the large energy of visible photons requires considering the possibility of excited state absorption (ESA) into energy levels of the  $4f^15d^1$  configuration of Pr<sup>3+</sup>. The energetic position and splitting of the  $4f^15d^1$  states depend much stronger on the crystal field. In the CaF<sub>2</sub> host, it provides comparably low crystal field strengths, which results in an energetically higher position of the lower edge of the  $4f^15d^1$  absorption band.<sup>24</sup> Therefore, ESA into these levels from the upper laser level is not likely for the usual pump wavelengths of Pr<sup>3+</sup>:CaF<sub>2</sub>. On the other hand, the Stark multiplets  $^3P_0$ ,  $^3P_1$ ,  $^3P_2$  and  $^1I_6$  of Pr<sup>3+</sup> are energetically separated by less than 2000 cm<sup>-1</sup>. Thus, the Boltzmann population of the levels  $^3P_2$  and in particular  $^3P_1$  must be considered at room temperature, and thermal excitation inevitably plays an important role in lowering the QE.<sup>25</sup>

To summarize, Fig. 5(b) displays the radiative transition rate, cross relaxation rate, and multiphonon relaxation rate. The cross relaxation rate is calculated by the formula,  $W_{CR} = 1/\tau - 1/\tau_{rad} - W_{MPR}$ , using the experimental and radiative lifetime. It is evident that the insertion of  $\text{La}^{3+}$  as a co-dopant causes a dramatic drop in the cross relaxation rate and an increase in the radiative transition rate. The cross relaxation rate can still approach an order of  $10^4 \text{ s}^{-1}$ , which is equal to the intrinsic radiation rate, even though it has decreased by a far larger amount than the intrinsic transition rate. The cross relaxation rate that follows is essentially constant. This study demonstrates unequivocally that not all  $\text{Pr}^{3+}$  ions become emission centers when co-doping with 20%  $\text{La}^{3+}$ , that is, partially Pr-Pr clusters are replaced by Pr-La clusters.

### 3.2 Investigation of the variations in luminescence centers using low temperature spectroscopy and computational simulation

#### 3.2.1 Low temperature selective-site excitation and TRES.

As previously discussed, the addition of  $\text{Lu}^{3+}$  or  $\text{Yb}^{3+}$  as co-dopants appears to generate new cluster centers containing both codopants.<sup>7</sup> The analysis of low temperature absorption spectra offers essential information about these cluster centers. The low temperature absorption spectra of 0.6Pr:CaF<sub>2</sub> and 0.6Pr,1.0La:CaF<sub>2</sub> samples are shown in Fig. 6(a). The transition of  $^3\text{H}_4\text{-}^3\text{P}_2$  is of particular significance, since it is usually used for optical excitation of  $\text{Pr}^{3+}$  emission. The absorption spectrum of the singly  $\text{Pr}^{3+}$  doped sample is clearly different from the spectra recorded for the co-doped samples. The spectrum of the singly doped sample is characterized by several tiny peaks at 468 nm for the  $^3\text{H}_4\text{-}^3\text{P}_2$  transition, but the spectrum of the co-doped sample has a broad peak at the same wavelength. In case of the 0.6Pr:CaF<sub>2</sub>

sample, absorption spectra is dominated by 443.54 nm. As can be easily spotted, after co-doping with  $\text{La}^{3+}$ , new absorption lines at 440.66 nm emerge, which significantly increase while the line at 443.54 nm decrease. The contrast between the absorption spectra clearly demonstrates a distinct arrangement of the  $\text{Pr}^{3+}$  ions in the singly doped  $\text{Pr}^{3+}$ :CaF<sub>2</sub> crystal. These new lines are related to the new absorption center caused by the Pr-La cluster.

According to the symmetry considerations, splitting of the manifolds with  $J = 4$  is 4 for cubic symmetry. For manifolds with  $J = 0$ , it has a single Stark level. Nevertheless, only the lowest Stark level of  $^3\text{H}_4$  is occupied at low temperatures (77 K). In the event of a single site structure, a single absorption line is thus expected for the  $^3\text{H}_4\text{-}^3\text{P}_0$  transition. The symmetry of the  $\text{Ca}^{2+}$  site in CaF<sub>2</sub> is cubic ( $O_h$ ) but due to the presence of interstitial  $\text{F}_i^-$  ions that balances the charge mismatch between  $\text{Pr}^{3+}$  and  $\text{Ca}^{2+}$ , the local symmetry drops to  $C_{3v}$  or  $C_{4v}$ .<sup>17</sup> In the case of the Pr-Pr or Pr-La cluster, the symmetry can even be lower. The absorption spectra of 0.6Pr:CaF<sub>2</sub> and 0.6Pr,1.0La:CaF<sub>2</sub> contains roughly 19 and 9 lines, clearly confirming the presence of many sites. Each sharp line can be associated with a specific site with a well-defined symmetry while the broad line evidences a strong inhomogeneous broadening most likely related to Pr-La clusters.<sup>26</sup>

Then we utilized the 0.6Pr 1.0La sample on the selective spectrum displayed in Fig. 6(b), which shows that the 0.6Pr,1.0La sample has at least two distinct  $\text{Pr}^{3+}$  sites. Emission spectra excited at 440.66 nm show a new peak at 480.8 nm, whereas red traces show only the same peak at 484 nm when excited at 443.54 nm, demonstrating that the incorporation of  $\text{La}^{3+}$  as a co-dopant modifies the clustering structure, *i.e.* producing more new luminescence centers.<sup>27</sup>

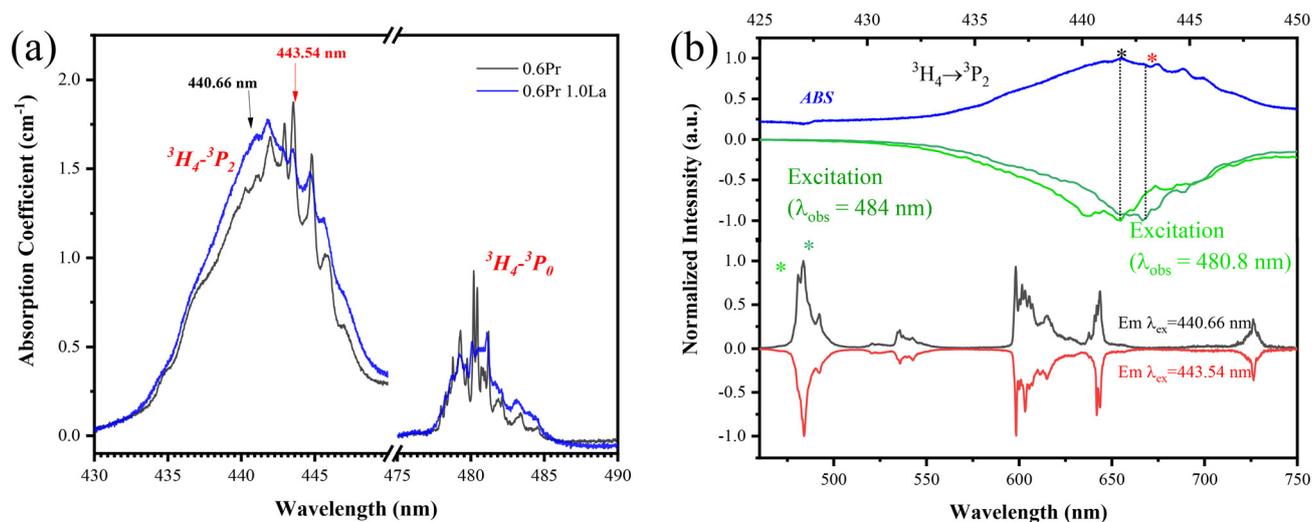


Fig. 6 (a) Absorption spectra of 0.6Pr:CaF<sub>2</sub> and 0.6Pr,1.0La:CaF<sub>2</sub> samples measured at 77 K; (b) comparison of absorption, emission and excitation spectra of the 0.6Pr,1.0La:CaF<sub>2</sub> sample. Blue lines are the absorption spectra. Black and red lines are the emission spectra that were excited via the absorption line marked with asterisk of the appropriate color. Green and olive traces represent the excitation lines that were measured observing emission from the lines marked by green or olive asterisks respectively. All the measurements have been done at 77 K.

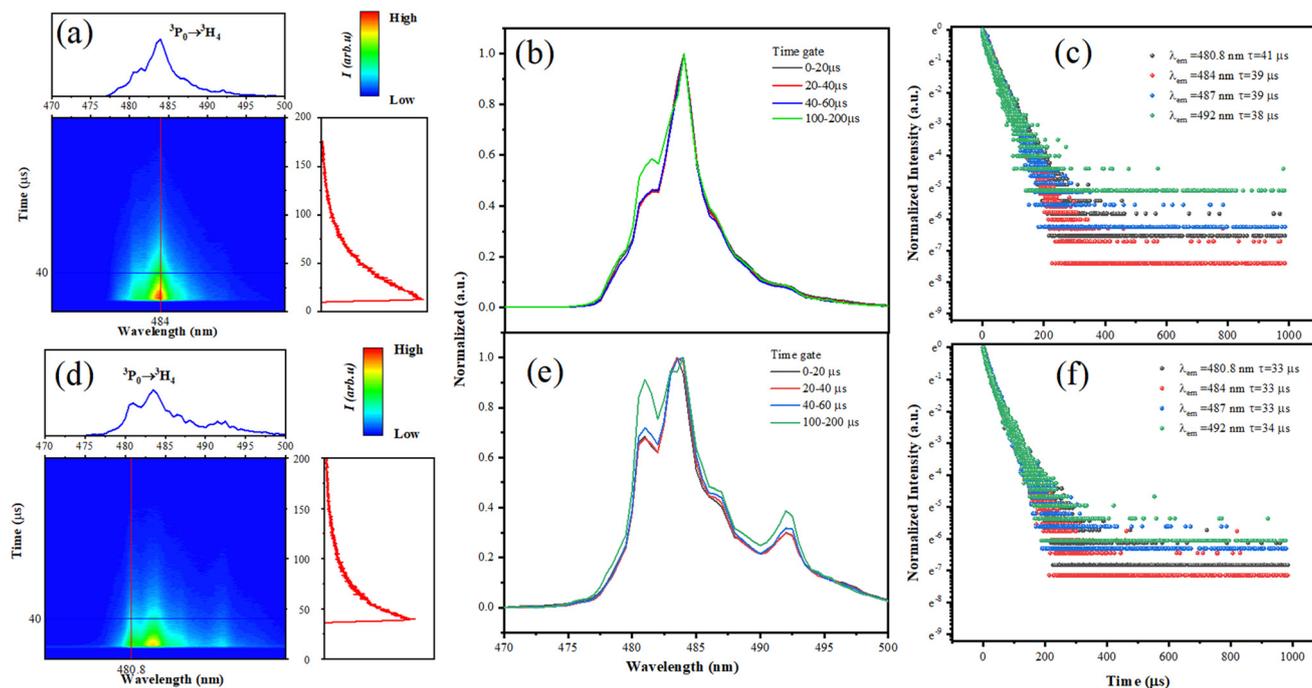


Fig. 7  $\text{Pr}^{3+}$  time-resolved spectra in 0.6Pr,1.0La:CaF<sub>2</sub> at 77 K. (a–c) Excited at 443.54 nm. (d–f) Excited at 440.66 nm. Colors from red to blue represent the logarithmic PL intensity from high to low. The time-resolved emission spectra (b and e) obtained with different time gates after pulse excitation. Time-resolve decays (c and f) at wavelengths of 480.8, 484, 487 and 492 nm.

In order to get better insight into luminescence processes present in that crystal, a series of liquid nitrogen time-resolved emission spectrum (TRES) measurements were performed. Recording the time-resolved emission spectrum with a time frame beginning at the end of the decay at 100  $\mu\text{s}$  allows one to isolate the emission spectrum associated with the slowest center, as shown in Fig. 7(b and e). The emission spectra integrated with different time gating are shown in Fig. 7(b). As can be easily seen, there is a distinct difference between green and other traces. This is due to the presence of several luminescence centres that should differ in decay kinetics. On the other hand, the decay curves displayed in Fig. 7(c) exhibit a few differences with almost identical lifetimes, which the DFT computation may account for given the little variations in the cluster configurations. The shorter the lifetime of the centre, the less pronounced it is in the spectra gathered longer after excitation pulse. The green spectrum is a mixture of long and short living centres. Black and red traces show emission spectra of long-lived centres. The emission spectrum of this first cluster (Fig. 7(b)) is characterized by an increased emission peak integrated from 100–200  $\mu\text{s}$  at 480.8 nm, which is consistent with the fact that the slowest decay was recorded at this wavelength (Fig. 7(c)). Another time window set during the first 20  $\mu\text{s}$  of the decay gives a very different emission spectrum. This new spectrum exhibits a prominent emission peak at 484 nm which is characteristic of the second  $\text{Pr}^{3+}$ - $\text{La}^{3+}$  cluster.

The existence of two types of  $\text{Pr}^{3+}$ - $\text{La}^{3+}$  clusters is convincingly confirmed by investigating the  $^3\text{P}_0$  time-resolved emission spectra in the co-doped samples at a low

temperature. In 0.6Pr,1.0La:CaF<sub>2</sub>, we observed the  $^3\text{P}_0$  decay at two distinct excitation wavelengths: 443.54 nm (Fig. 7(c)) and 440.66 nm (Fig. 7(f)). The decays ( $\tau_{\text{ex}443.54, \text{em}480.8} = 41 \mu\text{s}$ ) and ( $\tau_{\text{ex}440.66, \text{em}480.8} = 33 \mu\text{s}$ ) are different, suggesting the coexistence of two distinct clusters.

**3.2.2 Rare-earth cluster simulation of  $\text{Pr}^{3+}$  and  $\text{La}^{3+}$ .** When rare-earth ions are introduced into CaF<sub>2</sub>, they will replace the Ca<sup>2+</sup> ions and interstitial F<sub>i</sub><sup>-</sup> ions will work as charge compensation. There are multiple nonequivalent sites for the charge compensation F<sub>i</sub><sup>-</sup> ions to occupy. Subsequently, the 1|0|0|1<sub>1</sub> ( $C_{4v}$ ) and 1|0|0|1<sub>2</sub> ( $C_{3v}$ ) configurations with F<sup>-</sup> ions at the nearest and next-nearest sites of rare-earth ions respectively emerge.<sup>28</sup> These monomers further aggregate to form clusters. Based on ref. 29, the rare-earth clusters in the CaF<sub>2</sub> crystal are modeled and then fully relaxed. Fig. 8(a) and Table 2 display the possible clusters that are thermodynamically stable. Three groups of centers were identified: the first group consists of monomer centers, while the other groups are clusters with distinct local sublattices, namely cubic and square antiprisms. Within the  $\text{Pr}^{3+}$ :CaF<sub>2</sub> crystal, the nearest center  $C_{4v}$  configuration is more stable than  $C_{3v}$ , which is in agreement with the idea that large rare-earth ions like  $\text{Pr}^{3+}$  form small clusters.<sup>16</sup> Simultaneously, the nearest site center for  $\text{La}^{3+}$  that has almost the same ion radius as  $\text{Pr}^{3+}$  exhibits greater stability and conformity with the available data.<sup>28</sup> Formation energy of the clusters were plotted and illustrated in Fig. 8(b). The binding energy curve exhibits a piecewise variation as the number of  $\text{Pr}^{3+}$  increases. Low-order clusters with cubic sublattices are more easily generated than higher-order square antiprisms due to

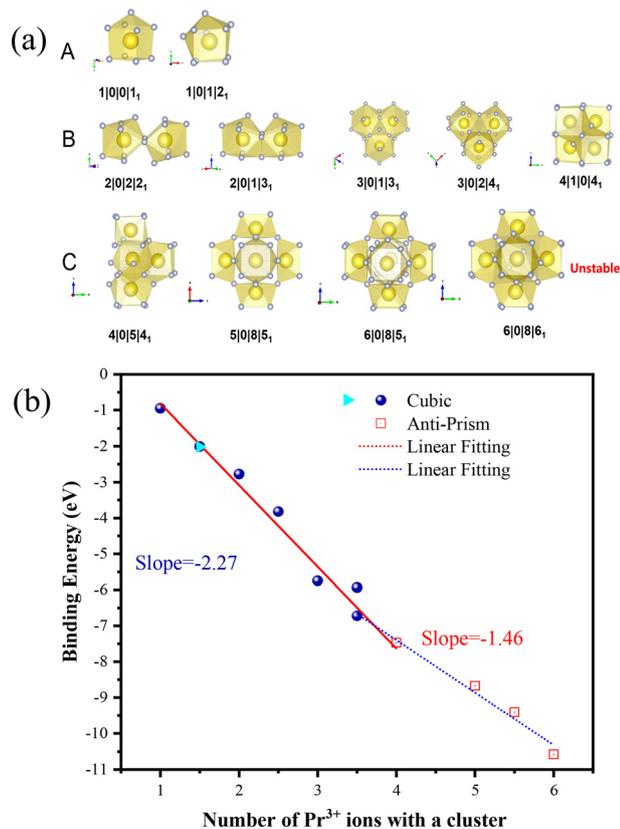


**Fig. 8** (a) The thermodynamically stable clusters in  $\text{Pr}^{3+}$  doped  $\text{CaF}_2$  crystals, and these centers are divided into three groups: “A”, “B”, and “C” stand for cubic monomers, cubic sublattice clusters, and square antiprism structure clusters, respectively. (b) The formation energy of the thermodynamically stable centers depends on the number of rare earth ions. The cyan triangles and blue circles represent two different types of cubic cluster configurations with distinct binding energies.

their binding energy slope ( $-2.27$  eV) being significantly larger than that of high-order clusters ( $-1.46$  eV).

Additionally,  $[\text{Pr}^{3+}\text{-La}^{3+}]$  clusters were simulated and shown in Fig. 9(a).  $\text{Pr}^{3+}$  and  $\text{La}^{3+}$  also have a tendency to

**Table 2** Formation energy of the thermodynamically stable  $\text{Pr}^{3+}$  and  $\text{La}^{3+}$  clusters in  $\text{CaF}_2$  crystals. The formation energy of  $\text{La}^{3+}$  centers is taken from ref. 28

Symbols	$\text{Pr}^{3+}$ centers (eV)	$\text{La}^{3+}$ centers (eV)
1 0 0 1 <sub>1</sub>	-0.951	-0.896
1 0 1 2 <sub>1</sub>	-2.005	-1.158
2 0 2 2 <sub>1</sub>	-2.019	-2.393
2 0 1 3 <sub>1</sub>	-2.774	-3.056
3 0 1 3 <sub>1</sub>	-3.819	-4.488
3 0 2 4 <sub>1</sub>	-5.748	—
4 1 0 4 <sub>1</sub>	-6.720	-5.513

group together to form  $[m\text{La}^{3+}\text{-}n\text{Pr}^{3+}]$  clusters. When more  $\text{Pr}^{3+}$  ions were added to the host, the bonding energy of the  $[\text{Pr}^{3+}\text{-La}^{3+}]$  clusters dropped linearly as shown in Fig. 9(b). It is observed that the formation energy of the Pr-La center is lower than that of the  $\text{Pr}^{3+}$  or  $\text{La}^{3+}$  clusters on the condition that  $m + n \leq 2$ , indicating that the former are more stable than the latter. On the other hand, when  $m + n > 2$ , the formation energy of the Pr-La center is significantly larger than that of the  $\text{Pr}^{3+}$  or  $\text{La}^{3+}$  clusters indicating that self-clusters may form at high concentrations.

In this part, to further elucidate the evolution of the local cluster structures in the Pr:CaF<sub>2</sub> crystals, we have carried out first-principles calculations. The results reveal that the cluster configurations are predominantly based on the cubic sublattice structure, and the higher-order prism configurations are not as stable, as evidenced by the shallower slope in the second stage of the binding energy trends. Interestingly, the cluster characteristics in the Pr-La co-doped samples still maintain the features of the cubic sub-lattice-based structure, which also helps explain the similarity in the lifetimes of the two Pr-La centers observed in the time-resolved spectroscopy.

## 4. Conclusion

The investigation of  $\text{Pr}^{3+}$ ,  $\text{La}^{3+}$  co-doped  $\text{CaF}_2$  samples shows a drastic increase of the number of luminescent  $\text{Pr}^{3+}$  ions as

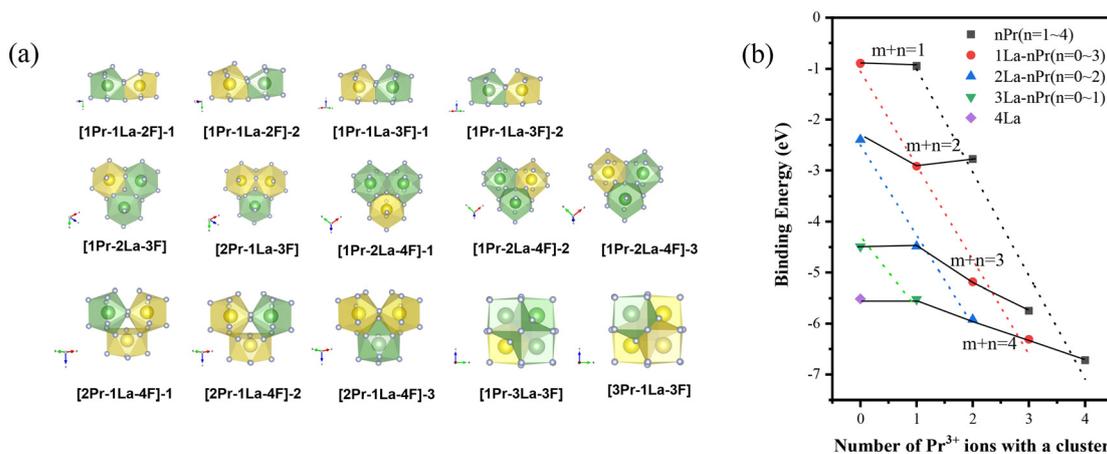


**Fig. 9** (a) The thermodynamically stable  $[\text{Pr}^{3+}\text{-La}^{3+}]$  centers in  $\text{CaF}_2$  crystals. (b) The formation energy of  $\text{Pr}^{3+}$  and  $\text{La}^{3+}$  clusters in relation to the quantity of  $\text{Pr}^{3+}$  ions present in each cluster.

opposed to singly doped  $\text{Pr}^{3+}:\text{CaF}_2$  where non-luminescent  $\text{Pr}^{3+}$  clusters predominate. An increase in  $\text{Pr}^{3+}$  luminescence by a factor of 231 is observed in  $0.6\text{Pr},20\text{La}:\text{CaF}_2$ , suggesting that the clusters encompassing  $\text{Pr}^{3+}$  and  $\text{La}^{3+}$  ions have replaced  $\text{Pr}^{3+}$  clusters. Two types of  $\text{Pr}^{3+}-\text{La}^{3+}$  clusters is convincingly confirmed by investigating the  $^3\text{P}_0$  time-resolved emission spectra in the co-doped samples at a low temperature. The computational results revealed that the addition of  $\text{La}^{3+}$  to the  $\text{Pr}^{3+}:\text{CaF}_2$  crystal results in clusters of  $[\text{mLa}^{3+}-\text{nPr}^{3+}]$ , with the formation energy decreasing with  $m+n$ . The first coordination shell of  $\text{Pr}^{3+}$  maintains a cubic structure, and the formation energy of the Pr-La center is larger than that of  $\text{Pr}^{3+}$  or  $\text{La}^{3+}$  clusters, suggesting self-cluster formation at high concentrations.

## Data availability

The data that support the findings of this study are available from the corresponding author, L. Su, upon reasonable request.

## Conflicts of interest

There is no conflict of interest in this manuscript.

## Acknowledgements

This work has been financially supported by the National Key Research and Development Program of China (2021YFE0104800), the National Natural Science Foundation of China (61925508, 62205359), and the Science and Technology Commission of Shanghai Municipality (23511102700). This work was also supported by the CAS Project for Young Scientists in Basic Research (YSBR-024).

## Notes and references

- D.-T. Marzahl, F. Reichert, P. W. Metz, M. Fechner, N.-O. Hansen and G. Huber, *Appl. Phys. B: Lasers Opt.*, 2014, **116**, 109–113.
- Z. Yang, S. Z. Ud Din, P. Wang, C. Li, Z. Lin, J. Leng, J. Liu, L. Xu, Q. Yang and X. Ren, *Opt. Laser Technol.*, 2022, **148**, 107711.
- Z. Yang, Q. Yang, X. Ren, Y. Tian, Y. Zu, C. Li, S. Z. U. Din, J. Leng and J. Liu, *Opt. Express*, 2022, **30**, 2900–2908.
- L. B. Zhou, J. Y. Zou, W. X. Zheng, T. Zhang, B. Xu, X. D. Xu, A. A. Lyapin and J. Xu, *Opt. Laser Technol.*, 2022, **145**, 107471.
- H. Yu, D. Jiang, F. Tang, L. Su, S. Luo, X. Yan, B. Xu, Z. Cai, J. Wang, Q. Ju and J. Xu, *Mater. Lett.*, 2017, **206**, 140–142.
- C. Xu, W. Wang, Z. Zhang, F. Ma, D. Jiang, A. Strzep, W. Zheng, B. Xu, H. Kou, J. Xu and L. Su, *Opt. Laser Technol.*, 2024, **168**, 109768.
- D. Serrano, A. Braud, J. L. Doualan, P. Camy and R. Moncorgé, *J. Opt. Soc. Am. B*, 2012, **29**, 1854–1862.
- D. R. Tallant, D. S. Moore and J. C. Wright, *J. Chem. Phys.*, 2008, **67**, 2897–2907.
- M. J. Weber and R. W. Bierig, *Phys. Rev.*, 1964, **134**, A1492–A1503.
- S. D. McLaughlan, *Phys. Rev.*, 1966, **150**, 118–120.
- S. A. Kazanskii, A. I. Ryskin, A. E. Nikiforov, A. Y. Zaharov, M. Y. Ougrumov and G. S. Shakurov, *Phys. Rev. B: Condens. Matter Mater. Phys.*, 2005, **72**, 014127.
- R. J. Booth, M. R. Mustafa and B. R. McGarvey, *Phys. Rev. B: Solid State*, 1978, **17**, 4150–4159.
- J. Fontanella and C. Andeen, *J. Phys. C: Solid State Phys.*, 1976, **9**, 1055.
- F. Ma, Z. Zhang, D. Jiang, Z. Zhang, H. Kou, A. Strzep, Q. Tang, H. Zhou, M. Zhang, P. Zhang, S. Zhu, H. Yin, Q. Lv, Z. Li, Z. Chen and L. Su, *Cryst. Growth Des.*, 2022, **22**, 4480–4493.
- J. Corish, C. R. A. Catlow, P. W. M. Jacobs and S. H. Ong, *Phys. Rev. B: Condens. Matter Mater. Phys.*, 1982, **25**, 6425–6438.
- B. M. Tissue and J. C. Wright, *Phys. Rev. B: Condens. Matter Mater. Phys.*, 1987, **36**, 9781–9789.
- F. Ma, F. Su, R. Zhou, Y. Ou, L. Xie, C. Liu, D. Jiang, Z. Zhang, Q. Wu, L. Su and H. Liang, *Mater. Res. Bull.*, 2020, **125**, 110788.
- A. Sottile, E. Damiano and M. Tonelli, *Opt. Lett.*, 2016, **41**, 5555–5558.
- G. P. Morgan, D. L. Huber and W. M. Yen, *J. Lumin.*, 1986, **35**, 277–287.
- B. Zandi, L. D. Merkle, J. B. Gruber, D. E. Wortman and C. A. Morrison, *J. Appl. Phys.*, 1997, **81**, 1047–1054.
- S. Normani, A. Braud, R. Soulard, J. L. Doualan, A. Benayad, V. Menard, G. Brasse, R. Moncorgé, J. P. Goossens and P. Camy, *CrystEngComm*, 2016, **18**, 9016–9025.
- J. M. F. v. Dijk and M. F. H. Schuurmans, *J. Chem. Phys.*, 1983, **78**, 5317–5323.
- S. Khiari, M. Velazquez, R. Moncorgé, J. L. Doualan, P. Camy, A. Ferrier and M. Diaf, *J. Alloys Compd.*, 2008, **451**, 128–131.
- H. Tanaka, S. Kalusniak, M. Badtke, M. Demesh, N. V. Kuleshov, F. Kannari and C. Kränkel, *Prog. Quantum Electron.*, 2022, **84**, 100411.
- S.-h. Huang, X.-j. Wang, B.-j. Chen, D. Jia and W. M. Yen, *J. Lumin.*, 2003, **102–103**, 344–348.
- R. H. Petit, P. Evesque and J. Duran, *J. Phys. C: Solid State Phys.*, 1981, **14**, 5081.
- S. A. Payne, J. A. Caird, L. L. Chase, L. K. Smith, N. D. Nielsen and W. F. Krupke, *J. Opt. Soc. Am. B*, 1991, **8**, 726–740.
- J. Liu, Y. Wang, Z. Zhang, Z. Zhang, D. Jiang, F. Tang, H. Kou, F. Ma and L. Su, *Opt. Mater. Express*, 2023, **13**, 2288–2301.
- C. R. A. Catlow, *J. Phys. C: Solid State Phys.*, 1973, **6**, L64.